The New French Operational Radar Rainfall Product. Part I: Methodology

P. TABARY

Centre de Météorologie Radar, Direction des Systèmes d'Observation, Météo-France, Trappes, France

(Manuscript received 26 October 2005, in final form 27 September 2006)

ABSTRACT

A new radar-based rainfall product has been developed at Météo-France and is currently being deployed within the French operational Application Radar à la Météorologie Infra-Synoptique (ARAMIS) radar network. The rainfall product is based entirely on radar data and comprises the following successive processing steps: 1) dynamic identification of ground clutter based on the pulse-to-pulse fluctuation of the radar signal, 2) reflectivity-to-rain-rate conversion using the Marshall–Palmer Z–R relationship, 3) correction for partial beam blocking using numerical simulations of the interaction between the radar wave and the terrain, 4) correction for vertical profile of reflectivity (VPR) effects based on ratio curves and a priori climatology-based VPR candidates, 5) correction for nonsimultaneity of radar measurements by making use of a cross-correlation advection field, 6) weighted linear combination of the corrected reflectivity measurements gathered at the various elevation angles of the volume coverage pattern, and 7) production of a 5-min rain accumulation using the advection field to mitigate undersampling effects. In addition to the final Cartesian, 512 km $\times$ 512 km, 1 km^2 in resolution, radar rainfall product, a map of quality indexes is automatically generated that allows for assessing empirically the accuracy of the estimation. This new product has been validated using 27 episodes observed during the autumns of 2002 and 2003 and the winter of 2005 by three S-band radars of the network. This paper is entirely devoted to the description of the methodology.

1. Introduction

Accurate rainfall estimates are crucial for numerous applications in hydrology, nowcasting, and mesoscale model validation. Ground-based operational weather radar networks are currently considered the only instruments capable of providing the requested high-resolution (1 km^2) and frequent (5 min) precipitation fields over mesoscale or even synoptic areas. The density of automated rain gauge networks is in general too scarce, especially in complex terrain, to yield the same space–time coverage of precipitation systems. On the other hand, rainfall estimation from satellite-borne instruments (radiometers or radars) is still an open field of research and does not fulfill as of yet the above-mentioned user's needs. The forthcoming Global Precipitation Mission will probably open new perspectives but it is likely going to take another decade or two before operational products become available.

While radars were recognized early on as key tools for monitoring the structure and evolution of precipitating systems, the correct understanding and assessment of the various error sources are more recent. Errors affecting the measurements of rainfall by radars can be grouped into three categories (Zawadzki 1984; Joss and Lee 1995; Dinku et al. 2002): 1) errors related to the radar system itself (radar hardware calibration, errors in the azimuth and elevation angles), 2) errors related to the interaction between the radar wave and the environment (ground clutter or biological targets, clear-air echoes, partial beam blocking, partial beam filling, attenuation by rain, filtering along the vertical due to beam broadening with range), 3) errors occurring when converting instantaneous radar reflectivity plan position indicators (PPIs) into surface rainfall accumulations [nonuniform vertical profile of reflectivity (VPR), wave propagation fluctuations, precipitation type, Z–R relationship, precipitation drift, advection of rain patterns]. The present paper reports on the development of the new French operational radar rainfall estimation algorithm that purports to correct radar data for ground clutter (GC), partial beam blocking (MSK), VPR effects (VPR), and advection (ADV). Radar

Corresponding author address: Pierre Tabary, Centre de Météorologie Radar, Direction des Systèmes d'Observation, Météo-France, 7, rue Teisserenc-de-Bort, 78195 Trappes, France. E-mail: pierre.tabary@meteo.fr

DOI: 10.1175/WAF1004.1

hardware and pointing angle calibration procedures are not considered in this paper [see Tabary (2003) for more information on that]. Likewise, as all 18 French operational radars are conventional ones, departures from the Marshall–Palmer Z–R relationship ($Z = 200R^{1.6}$) and attenuation by rain are not corrected for. Polarimetry appears to be a very promising way of dealing with these two effects (Testud et al. 2000) and Météo-France is engaged in a multiyear evaluation of this new technology (Parent-du-Chatelet and Guiméra 2003). Finally, the processing chain described in this paper does not perform any real-time radar–rain gauge adjustment (Fulton et al. 1998; Anagnostou and Krajewski 1999). Such an adjustment is not excluded in the real-time postprocessing stage in order to mitigate calibration biases but it is often considered preferable to first go as far as possible in the correction of the radar data errors.

Following the pioneering work of Joss and Lee (1995), the radar rainfall estimation algorithm is modular and consists of a series of steps that attempt to correct the raw radar PPIs of the volume coverage pattern (VCP) successively for the four identified sources of error (GC, MSK, VPR, and ADV) and then combine them optimally on a pixel-by-pixel basis to obtain the best 5-min surface rainfall accumulation. The originality of the method relies on the fact that each radar PPI of the VCP has a companion PPI that is updated after each step of the processing, which indicates empirically the quality of each pixel (a real value ranging between 0 and 1). This can be viewed as a simplified, operationally oriented version of the concept of hydrologic visibility recently introduced by Pellarin et al. (2002). The final weighted linear combination of the set of available PPIs is achieved by taking the final quality PPIs as weighing factors. The final quality PPIs are also useful indicators of the pixel-by-pixel quality of the radar rainfall product, which is essential information for a large number of applications (assimilation by a flood forecasting model, elaboration of composite products, radar–rain gauge comparisons, etc.).

As the algorithm is meant to be deployed operationally on all radars within the French network, with different VCPs (one, two, three, or more elevation angles scanned every 5 min), different physical environments (plains and mountains), different antennas, and different wavelengths (S and C), special emphasis is placed on the robustness, simplicity, computational cost, and versatility of the processing chain. The French radar network, as well as the old and the new radar rainfall products, are described in section 2. The four modules (GC, MSK, VPR, and ADV) and the weighed linear combination are detailed and discussed in section 3. For each module, the correction scheme, the update formula for the weights, and the operational implementation are detailed and commented upon. The specific evaluation of the VPR identification module and the overall validation of the final quantitative precipitation estimation (QPE) product are addressed in a companion paper (Tabary et al. 2007, hereafter Part II).

2. The French radar network: Old and new radar rainfall products

The French Application Radar à la Météorologie Infra-Synoptique (ARAMIS) radar network was composed in 2004 of 18 radars. All of them were conventional, non-Doppler radars. Over the period 2004–07, all radars of the network will have been equipped with a triple pulse rise time (PRT) scheme for Doppler processing (Tabary et al. 2006). Over the same period, six new C-band Doppler, polarimetric radars will be installed bringing the total number of the radars of the network to 24. Figure 1 shows the geographical locations of the radars and Table 1 gives their main technical characteristics. The scanning strategy of the radars has been designed specifically for hydrological purposes and currently consists of typically three low-elevation scans every 5 min. Data are processed with a home-developed radar processor (Parent-du-Châtelet et al. 2001). This new processor is very versatile and allows for the production of a wide variety of images and products (polar–Cartesian, 250 to 500 m–1 km, instantaneous–accumulated, raw–clutter filtered, Doppler–polarimetric) as well as for controlling the antenna and getting real-time information on the status of each component of the radar system. The monitoring of the hardware calibration of the radars is carried out through a software program called ISURAD (Tabary 2003) that computes every day and for each radar the mean intensity of the closest ground-clutter targets and the mean radar–rain gauge bias. ISURAD also routinely performs radar–radar comparisons in overlapping areas. Cartesian, 512 km $\times$ 512 km, 1 km^2 in resolution, clutter-filtered, pseudo–constant altitude plan position indicator (CAPPI) reflectivity images are produced at each radar site every 5 min and then concentrated at the national center in Toulouse where composite products are elaborated and then disseminated to public and private users for nowcasting applications.

In the old radar QPE, pseudo-CAPPI reflectivity images were accumulated over 15 min using a cross-correlation advection field and the Marshall–Palmer Z–R relationship to yield rainfall amount maps. The

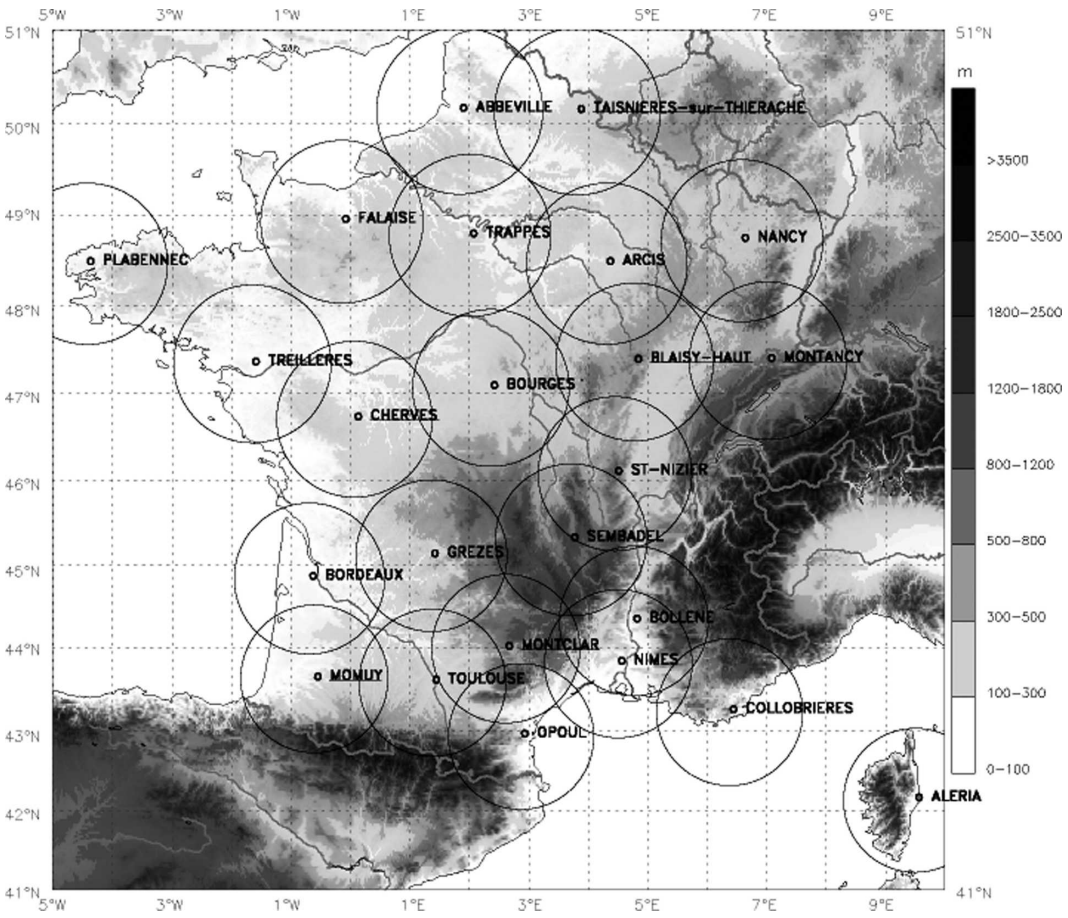

FIG. 1. Locations of the 24 radars of the French ARAMIS network in 2007. The radars that have been recently (2004–06) installed at new sites have their names underlined. Notice that the Trappes, Toulouse, and Montancy radars are equipped with dual-polarization capabilities. The 100-km-range circles, orography, main rivers, and political borders have all been superimposed.

current radar rainfall estimation algorithm does not include corrections for partial beam blocking or VPR effects. This results in systematic underestimations of the rainfall accumulations in some sectors of mountainous areas (mainly in the southeast of France) and at long range (beyond 100 km) and frequent overestimations due to the bright band in the cold season. The fact that the 2D reflectivity images are composited in a static, pseudo-CAPPI way induces a number of drawbacks such as VPR-related discontinuities at the transition distances between elevation angles and areas of permanent ground clutter. Pellarin et al. (2002) have shown that the rainfall accumulation estimation could be improved by compositing, in a static way, the image on a pixel-by-pixel basis.

An overview of the new radar rainfall algorithm is given in Fig. 2. The processing chain is made of seven successive modules: ground-clutter identification (GC), reflectivity-to-rain-rate conversion (ZR), partial beam-blocking correction (MSK), VPR correction (VPR), correction for advection (ADV), weighed linear combination (WLC), and 5-min rainfall accumulation (ACC). The input data are the reflectivity PPIs. Each reflectivity PPI of the VCP has a companion PPI that indicates the quality or weight of each pixel or, in other terms, its relevance with respect to the underlying surface rainfall. The quality index PPIs, denoted by $\omega_k(i, j)$ in Fig. 2, where k is the index of the elevation angle, are set to 1 in the beginning. In the course of the processing, their values are changed to account for the uncertainty in the corrections that are applied to the rainfall rates. For instance all clutter-classified pixels have their weights set to zero after the first module (GC). Likewise, pixels that have been corrected for partial beam blocking have their weight decreased to account for uncertainty in the correction.

The algorithm makes use of a number of a priori information sources: some are dynamic such as the

TABLE 1. Technical characteristics of the 24 operational radars of the French ARAMIS network. The six radars that have recently been deployed at new sites (Blaisy, Cherves, Momuy, Montancy, Montclar, and Taisnières) appear in boldface. The scan strategies correspond to the situation of the network in 2004. At that time, the scan strategies of the new radars was not yet finalized (hence the blank spaces in the table). Most scan strategies have been revisited since then. Notice that some radars perform the same tilt several times every 5 min (hence the repetition of the elevation angle). The distances (minimal and maximal) over which data at a given elevation are used in the pseudo-CAPPI image are indicated between parentheses after the value of the tilt. It is always the lowest tilt that is used at a long range. As an example, 0.4 (60–) means that the 0.40 elevation angle is used from 60 km up to the maximum radar range.

Radar location	Lat	Lon	Altitude of the antenna (m)	Band	3-dB beamwidth (°)	Operational elevation angles scanned every 5 min (°) [distance (km) over which data are used in the composite image]
Abbeville	50°08′13″N	1°50′09″E	83.6	C	1.25	0.4, 0.4, 0.4 (0–)
Aléria	42°07′51″N	9°29′51″E	63.6m	S	1.28	4.0 (west), 1.4 (east, 0–35), 1.0 (east, 35–70), 0.6 (east, 70–)
Arcis	48°27′47″N	4°18′38″E	165.7	C	1.1	0.4, 1.1 (0–60), 0.4 (60–)
Blaisy-Haut	**47°21′23″N**	**4°46′39″E**	**607.2**	**C**	**1.1**	
Bollène	44°19′26″N	4°45′48″E	324.5	S	1.28	1.8 (0–36), 1.2 (36–76), 0.8 (76–)
Bordeaux	44°49′57″N	0°41′26″W	71	S	1.8	9.0 (0–12), 1.5 (12–50), 0.4 (50–)
Bourges	47°03′35″N	2°21′39″E	173	C	1.25	0.7, 0.7, 0.7 (0–)
Cherves	**46°41′59″N**	**0°04′01″E**	**174.2**	**C**	**1.1**	
Collobrières	43°13′03″N	6°22′26″E	653.7	S	1.28	1.6 (0–35), 1.2 (35–70), 0.8 (70–)
Falaise	48°55′41″N	0°08′53″W	166	C	1.1	0.4, 0.4, 0.4 (0–)
Grèzes	45°06′19″N	1°22′15″E	361	S	1.8	0.4, 1.0 (0–61), 0.4 (61–)
Momuy	**43°37′26″N**	**0°36′43″W**	**145.7**	**C**	**1.1**	
Montancy	**47°22′10″N**	**7°01′13″E**	**925.3**	**C**	**1.1**	
Montclar	**43°59′28″N**	**2°36′41″E**	**678.5**	**C**	**1.1**	
Nancy	48°43′00″N	6°34′57″E	297.2	C	1.25	0.7, 0.7, 0.7 (0–)
Nîmes	43°48′26″N	4°30′13″E	78	S	1.8	2.5 (0–22), 1.3 (22–80), 0.6 (80–)
Opoul	42°55′10″N	2°51′58″E	717.8	S	1.28	1.4 (0–55), 1.0 (55–100), 0.6 (100–)
Plabennec	48°27′43″N	4°25′43″W	111	S	1.28	1.3 (0–35), 0.7 (35–50), 0.4 (50–)
Saint Nizier	46°04′02″N	4°26′48″E	920	C	1.1	0.4, 0.4, 0.4 (0–)
Sembadel	45°17′28″N	3°42′38″E	1141	C	0.9	0.4, 0.4, 0.4 (0–)
Taisnières	**50°07′45″N**	**3°48′47″E**	**208.8**	**C**	**1.1**	
Toulouse	43°34′31″N	1°22′38″E	187	C	1.25	0.8, 1.4 (0–40), 0.8 (40–)
Trappes	48°46′29″N	2°00′32″E	191	C	1.1	0.4, 0.4, 0.4 (0–)
Treillières	47°20′12″N	1°39′09″W	80	C	1.25	0.4, 0.4, 0.4 (0–)

pulse-to-pulse reflectivity fluctuation PPIs that are used to discriminate ground clutter from precipitation in the GC module, the cross-correlation advection field (ADV and ACC), or the model-predicted freezing level height that is a key parameter of the VPR module. Some are more static such as the statistical ground-clutter PPIs, the occultation rate PPIs, the a and b parameters of the Z–R relationship, or the digital terrain map around the radar. Up to module 5 (ADV), rain-rate PPIs and quality index PPIs are updated sequentially module after module. In an operational context, it is much more convenient to work with separate modules because then it is very easy to inhibit or improve one of them without having to rethink the whole structure of the processing chain. From a physical point of view though, it is true that some modules ought to be coupled (MSK and VPR for instance). Module 6 (WLC) achieves the weighed linear combination of the set of available rain-rate PPIs. The weighing factors that are applied are the quality index PPIs. The quality of the 5-min rainfall accumulation maps can be documented by aggregating in some way the set of quality index PPIs (see the end of section 3).

3. Description and discussion of the successive processing steps

a. Ground-clutter identification

Ground-clutter identification is done quite satisfactorily at Météo-France by using the pulse-to-pulse fluctuation of the radar reflectivity (Sugier et al. 2002). So-called σ PPIs are produced in real time on the same Cartesian grid as the reflectivity PPIs. For the typical rotation rate of the French radars (5° s^{-1}), σ values are typically around 1 dB in ground-clutter areas, 5 dB in rain, and 3 dB in snow so that a discrimination threshold can easily be determined. When the antenna rotation rate exceeds 20° s^{-1}, the σ values of ground-clutter targets tend to spread over larger values and the scheme is a bit less effective with a number of ground-

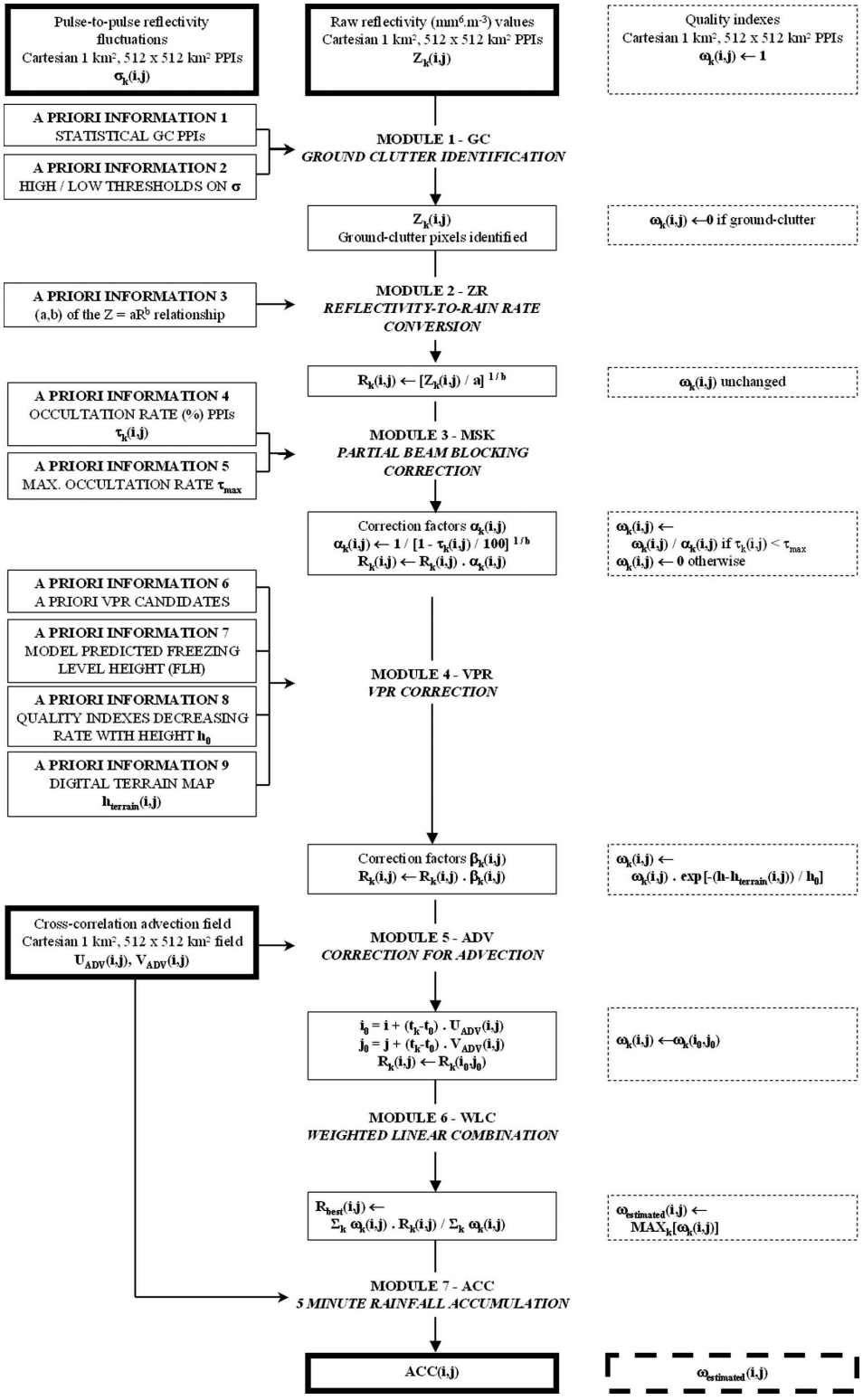

FIG. 2. Overview of the new radar rainfall algorithm.

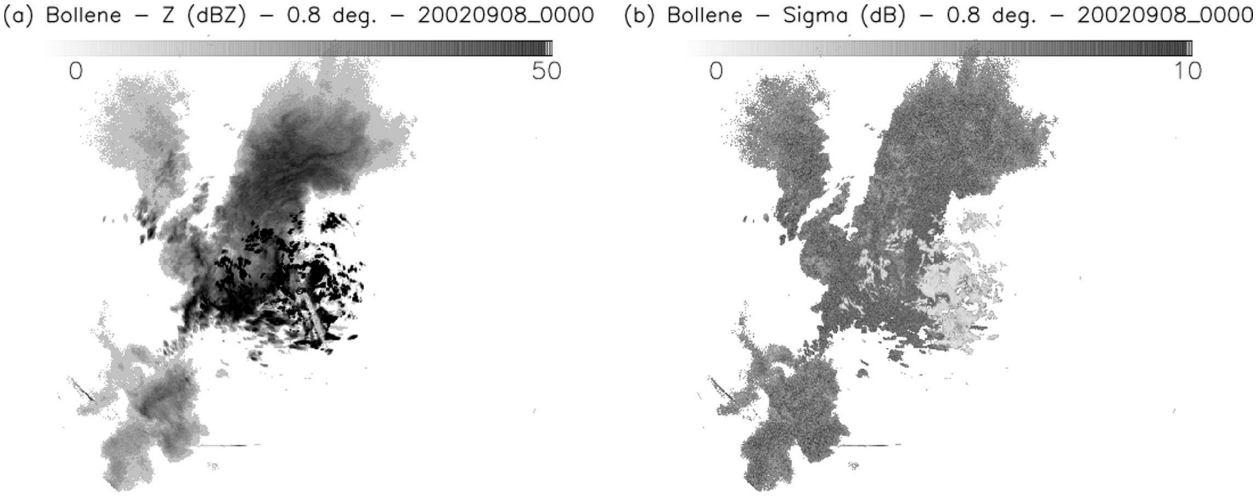

FIG. 3. (a) A raw reflectivity and (b) a σ PPI obtained with the Bollene radar at 0000 UTC 9 Sep 2002 at an 0.8° elevation angle.

clutter pixels being incorrectly classified as rain. The current introduction of Doppler and polarimetric capabilities within the radar network will undoubtedly contribute to improvements in the effectiveness of the ground-clutter identification procedure.

The σ-based ground-clutter identification scheme is fully dynamic and deals with abnormal propagation on the one hand and intense rain over ground clutter on the other hand.

Figure 3 shows an example of the potential of σ to discriminate between rain and ground clutter. Figures 3a and 3b are, respectively, a raw reflectivity and a σ PPI obtained with the Bollene radar at an elevation angle of 0.8° on 9 September 2002 at 0000 UTC. The radar is located in a mountainous environment and numerous strong cluttered pixels are noticeable on the reflectivity PPI in the vicinity of the radar. The σ PPI is bimodal with low values corresponding to ground clutter and higher values to rainy pixels.

Ground-clutter-classified pixels have their quality index set to zero, which simply means that they will nott be taken into account in the weighed linear combination.

b. Reflectivity-to-rain-rate conversion

The Z–R relationship that is used to convert radar reflectivity Z (mm^6 m^{-3}) to rain rate R (mm h^{-1}) is the Marshall–Palmer relationship:

$$Z = 200R^{1.6}. \quad (1)$$

In a future version of the radar rainfall algorithm, a stratiform–convective partition will be introduced and different Z–R relationships will be used according to the results of the classification. Likewise, polarimetric estimations of the rain rates at this point may be fed into the radar rainfall processing chain.

The quality index of each pixel is kept unchanged throughout this module.

c. Partial beam blocking correction

Using a high-resolution (250 m) Digital Terrain Model (DTM), the radar technical characteristics (wavelength, antenna diagram, transmitted power, etc.), and its sampling strategy (elevation angles), occultation rate PPIs are simulated following the approach proposed by Delrieu et al. (1995) and Pellarin et al. (2002). The simulation software reproduces the radar wave propagation in the atmosphere and its interaction with the terrain. A standard 4/3 earth radius model is assumed to compute the height of the radar beam as a function of range. The occultation rate PPIs (denoted in Fig. 2 and hereafter as $\tau_k(i, j)$ expressed in % of mm^6 m^{-3}) may then be used to correct the radar data on a pixel-by-pixel basis. Under the assumption that the radar reflectivity does not vary with height within the radar beam, the correction factors $\alpha_k(i, j)$ to be applied to the observed rain rates (mm h^{-1}) read

$$\alpha_k(i, j) = \{1/[1 - \tau_k(i, j)/100]\}^{(1/b)}, \quad (2)$$

where b is the exponent of the Z–R relationship. For the correction procedure to be efficient, it is very important that the azimuth angle and, to a lesser extent, the elevation angle of the radar be well calibrated. The application of the correction may indeed be quite detrimental in narrow masks and on the edges of large masks if the radar azimuth angle is biased. French radar azimuths are monitored operationally twice a day by comparing the sun signature of radar images with its

theoretical expected position given the location of the radar and the date and time. Experience shows that the radar azimuth positioning typically fluctuates by 0.1°.

At longer ranges, the assumption that the radar reflectivity does not vary with height within the radar beam becomes questionable. With a standard 1° beamwidth at −3 dB, the radar measurement represents a vertical integration over 1700 m at 100 km and 3400 m at 200 km. If the VPR is decreasing, as it is climatologically the case, then the actual correction factors will be underestimated. The amount of underestimation can be evaluated: let us assume that the actual reflectivity (dBZ) decreases linearly with height, with the decreasing rate (expressed in decibels per kilometer) being denoted by γ ($\gamma < 0$):

$$Z_{\mathrm{dB}}(h_1) = Z_{\mathrm{dB}}(h_0) + \gamma(h_1 - h_0), \tag{3}$$

where h_0 and h_1 are two arbitrary heights. Let also assume that the *one-way* antenna diagram is Gaussian:

$$P(\theta) = P_{\max} \exp\{-(\ln 2)[(\theta - \theta_C)/\Delta\theta]^2\}, \tag{4}$$

where $\Delta\theta$ is the half 3-dB beamwidth, θ_C the elevation of the center of the beam, and $P(\theta)$ the energy radiated at the elevation θ.

In the absence of partial beam blocking, the measured reflectivity $Z_{\mathrm{measured,NOMSK}}(\theta_C)$ at the elevation θ_C can be expressed as

$$Z_{\mathrm{measured,NOMSK}}(\theta_c) = \left[\int_{\theta=\theta_C-2\Delta\theta}^{\theta=\theta_C+2\Delta\theta} Z(\theta)P^2(\theta)\,d\theta\right] \Bigg/ \left[\int_{\theta=\theta_C-2\Delta\theta}^{\theta=\theta_C+2\Delta\theta} P^2(\theta)\,d\theta\right], \tag{5}$$

where $Z(\theta)$ is the reflectivity introduced in Eq. (3) and expressed in linear units (mm^6 m^{-3}) . In Eq. (5), the integration was arbitrarily limited to $[-2\Delta\theta, +2\Delta\theta]$.

Consider now the case of partial beam blocking and let θ_0 be the blocking elevation, that is, the elevation below which no energy is received from the radar transmitter. Here, θ_0 is related to the *geometrical* reflectivity occultation rate τ, arising from the numerical simulation (i.e., assuming that the VPR does not change inside the radar beam), as follows:

$$\tau = 100\left[1 - \frac{\displaystyle\int_{\theta_0}^{\theta_c+2\Delta\theta} P^2(\theta)\,d\theta}{\displaystyle\int_{\theta_c-2\Delta\theta}^{\theta_c+2\Delta\theta} P^2(\theta)\,d\theta}\right], \tag{6}$$

with the convention $\tau = 0\%$ in the absence of partial beam blocking and τ 100% when the beam is totally blocked. The measured reflectivity $Z_{\mathrm{measured,MSK}}$ can be written as

$$Z_{\mathrm{measured,MSK}}(\theta_c) = \left[\int_{\theta=\theta_0}^{\theta=\theta_C+2\Delta\theta} Z(\theta)P^2(\theta)\,d\theta\right] \Bigg/ \left[\int_{\theta=\theta_C-2\Delta\theta}^{\theta=\theta_C+2\Delta\theta} P^2(\theta)\,d\theta\right]. \tag{7}$$

The correct rain-rate correction factor α is then equal to

$$\alpha = \left(\frac{Z_{\mathrm{measured,NOMSK}}}{Z_{\mathrm{measured,MSK}}}\right)^{1/b}. \tag{8}$$

The vertical variation of the actual reflectivity (dBZ) at the range r from the radar can be expressed as a function of the elevation angle,

$$\begin{aligned} Z_{\mathrm{dB}}(\theta) &= Z_{\mathrm{dB}}(\theta_C) + \gamma r[\sin(\theta) - \sin(\theta_C)] \\ &\approx Z(\theta_C) + \gamma r(\theta - \theta_C), \end{aligned} \tag{9}$$

if one assumes low (θ, θ_C) elevation angles. Introducing Eq. (9) into Eqs. (5) and (7) and simplifying by $Z(\theta_C)$ at the numerator and denominator yields the following equation for α:

$$\alpha = \left[\frac{\displaystyle\int_{\theta_C-2\Delta\theta}^{\theta_C+2\Delta\theta} P^2(\theta)10^{\gamma r(\theta-\theta_C)/10}\,d\theta}{\displaystyle\int_{\theta_0}^{\theta_C+2\Delta\theta} P^2(\theta)10^{\gamma r(\theta-\theta_C)/10}\,d\theta}\right]^{1/b}, \tag{10}$$

where b is the Z–R relationship exponent.

Equations (4), (6), and (10) can be used to compute the correct rain-rate correction factor in the presence of

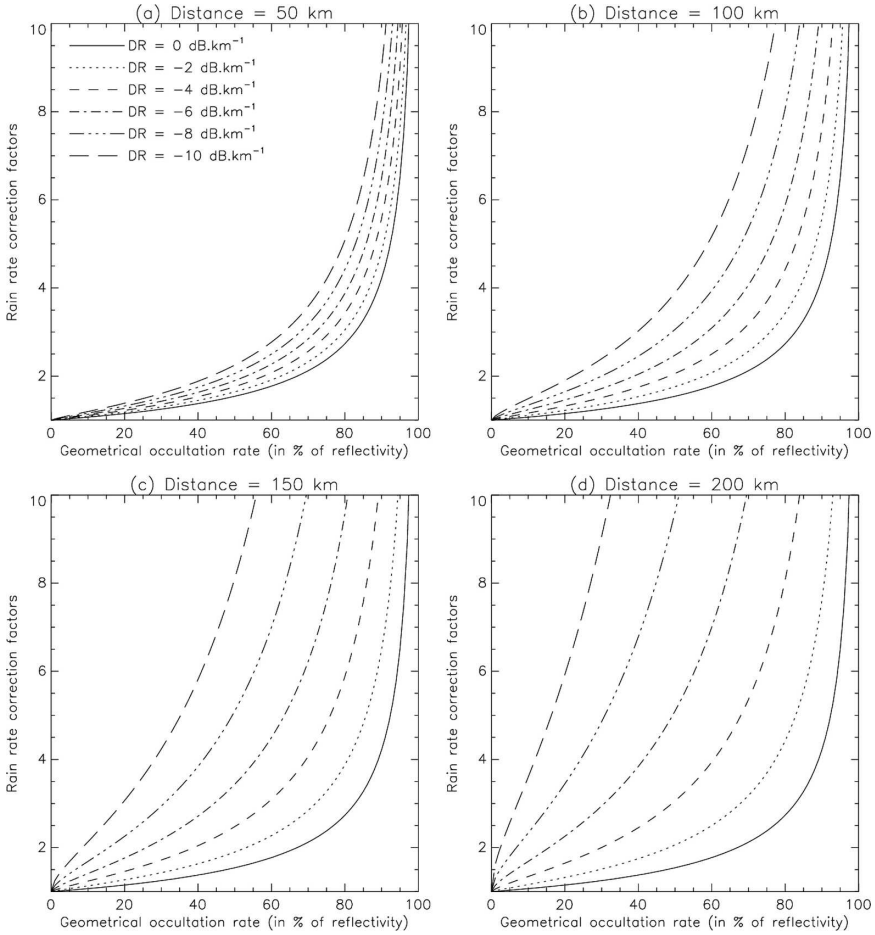

FIG. 4. Illustration of the effect of a nonuniform VPR on partial beam blockage correction factors.

partial beam blocking and a nonuniform VPR. The resulting α depends upon the geometrical reflectivity occultation rate (τ), the reflectivity decreasing rate (γ), and the distance to the radar (r).

Figure 4 presents the curves $\alpha(\tau)$ obtained at four different ranges (50, 100, 150, and 200 km) and for different reflectivity decreasing rates (0, −2, −4, −6, −8, and −10 dB km^{-1}). The rain-rate correction factors under the assumption of a uniform VPR are obtained for $\gamma = 0$ dB km^{-1} (solid lines in Fig. 4). All α curves in Fig. 4 are increasing functions of the reflectivity occultation rate (τ), the reflectivity decreasing rate (γ), and the range (r). Consider, for example, the case of a geometrical occultation rate equal to 50%; that is, half of the beam is intercepted by the orography. The rain-rate correction factor α for a uniform VPR is equal to about 1.5 whatever distance is considered. For a gently decreasing VPR ($\gamma = -2$ dB km^{-1}), α varies from 1.6 at 50 km to 1.9 at 200 km. For γ equal to −4 dB km^{-1}, which is the climatological value in France (see Part II), α ranges from 1.7 at 50 km to 3 at 200 km. In the extreme case when the VPR is very rapidly decreasing ($\gamma = -10$ dB km^{-1}) and the range is equal to 200 km, the actual α is close to 10 times the value of the basic, geometrical α. This analysis clearly demonstrates the impact of a nonuniform VPR on the partial beam-blocking correction factors. However, taking into account VPR effects in an operational beam blockage correction scheme would require, for the correction never to be detrimental, knowledge of the VPR in real time everywhere in the domain with a high degree of confidence. Despite a few promising attempts (Vignal et al. 2000), retrieval of the spatial structure of the VPR in real time is still beyond our reach with a single radar, especially at long ranges. We consequently considered it wiser for a first version of the new radar rainfall product to neglect VPR effects in the partial beam-blocking correction procedure. Another argument for doing so in operations is that the correction factors are limited to a maximum value of $\alpha = (1 - \tau_{\max}/100)^{-1/b} = 2.12$,

where $\tau_{max} = 70\%$ is the maximum value up to which shielded data can be corrected (see below). When the impact of the VPR is included, the resulting correction factors can be as large as 20 (see Fig. 4) and one must be very confident to apply such enhancement factors to measurements in an operational context. Further studies may demonstrate that the use of a horizontally uniform VPR, such as the one retrieved in the VPR module, is already helpful in accounting for VPR effects on beam blockage correction and improves the rain-rate estimation. If so, this will be introduced in a subsequent version of the radar rainfall product.

The updated formula for the quality indexes should reflect the fact that there is more uncertainty for the values of the correction factors for large occultation rates than for smaller ones. This uncertainty arises from the fact that the DTM-based simulations rely on a number of assumptions (e.g., propagation condtions, interaction between the radar wave and the terrain, etc.) and data (resolution of the DTM, antenna diagram) that may not always accurately reproduce the actual beam blockage process and that VPR effects are taken into consideration. A Monte Carlo approach, consisting of letting all the parameters in the simulation vary within reasonable predetermined ranges could be used to empirically assess the variance of the correction factors as a function of the mean occultation rate. This has not been done in the present study. The following formulas are proposed:

$$\omega_k(i,j) \leftarrow \omega_k(i,j)/\alpha_k(i,j) = \omega_k(i,j)/\{1/[1 - \tau_k(i,j)/100]\}^{(1/b)} \quad \text{if} \quad \tau_k(i,j) < 70\% \quad \text{and} \tag{11}$$

$$\omega_k(i,j) \leftarrow 0 \quad \text{if} \quad \tau_k(i,j) > 70\%. \tag{12}$$

Data shielded by more than 70% have their weights set to zero, which means that they will not be included in the final rainfall rate estimation. This threshold was obtained by Dinku et al. (2002). For occultation rates smaller than 70%, the weight is simply inversely proportional to the rain-rate correction factor. For occultation rates of 20%, 50%, and 70%, the rain-rate correction factors are, respectively, equal to 1.15, 1.54, and 2.12 and the corresponding weights are, respectively, multiplied by 0.87, 0.65, and 0.47.

d. VPR correction

Very early on the VPR was recognized as being one of the most important sources of errors in radar rainfall estimations (Zawadzki 1984). Bright bands often lead to a significant overestimation of rainfall accumulation in stratiform rain while radar-derived rainfall amounts are usually underestimated at long range due to the height of the beam. Many operational services have introduced real-time VPR identification and correction procedures (Koistinen 1991; Kitchen et al. 1994; Joss and Lee 1995; Kitchen 1997; Fulton et al. 1998; Novak and Kracmar 2001; Germann and Joss 2002). Most of those methods rely on volumetric data, which allow for the retrieval of the apparent VPR in the vicinity of the radar where all levels are well observed by the radar. Then, according to the complexity of the method, this apparent VPR is further refined by taking into account the radar beam characteristics. The so-called identified VPR, assumed to be uniform horizontally, is finally used everywhere in the radar domain to extrapolate the PPI measurements down to ground level.

As mentioned in the introduction, the French operational radars typically scan a limited number of elevation angles every 5 min and a direct observation of the VPR at close range from the radar is not possible. Therefore, the VPR identification and correction module (VPR) follows—though in a simplified manner—the approach proposed by Andrieu and Creutin (1995) and Andrieu et al. (1995). It relies on the calculation of ratios between hourly rainfall accumulations gathered at different elevation angles and on a conceptualization of the VPR that allows defining a limited number of candidates as in Kitchen (1997). It takes into account exactly the filtering of the profile induced by the radar beam. The advantage of using ratios is that the only assumption that is needed is that there is a separation between horizontal and vertical variations of the 3D rainfall field:

$$R(x,y,z) = R_{\text{ground}}(x,y)\text{VPR}_{\text{app}}(z), \tag{13}$$

where R_{ground} is the rainfall rate at ground level and $\text{VPR}_{\text{app}}(z)$ the apparent normalized rain-rate profile. The computation of ratios between rain rates or, equivalently, rainfall accumulations gathered at different elevation angles, say θ_{LOW} and θ_{UPP}, allows for the cancellation of the horizontal variation while revealing valuable information about the vertical structure:

$$R(x,y,\theta_{\text{UPP}})/R(x,y,\theta_{\text{LOW}}) = \text{VPR}_{\text{app}}(z_{\text{UPP}})/\text{VPR}_{\text{app}}(z_{\text{LOW}}), \tag{14}$$

where z_{LOW} and z_{UPP} are the beam heights corresponding to θ_{LOW} and θ_{UPP}. From there on, two difficulties need to be addressed: first, the true VPR has to be retrieved from the apparent VPR by taking into account the antenna diagram. Second, ratios only provide indirect information on the structure of the VPR because the altitude of the radar beam at any elevation angle steadily increases with range. The methodology described hereafter deals with those two difficulties simultaneously. The various steps of the identification procedure are described in a very precise and detailed manner to allow for reproduction by any other operational service.

1) STEP 1: COMPUTATION OF HOURLY RAIN-RATE-RATIO CURVES

Every 5 min, rain-rate data at each tilt (θ_k, $k = 1, \ldots, N_{PPI}$) of the VCP are accumulated over the past hour. Then data are integrated in the azimuth so as to provide radial accumulation curves [$\Re_{ACC}(\theta_k, r)$] with a range resolution of 1 km. The curves are limited to $r_{max} = 150$ km because propagation fluctuations and beam filtering make the quantitative use of radar data beyond that range questionable. Only data with a strictly positive weights [$\omega_k(i, j) > 0$) are taken into account in the space–time integration. This allows us to discard clutter-classified and strongly shielded pixels.

A total of $N_{PPI}(N_{PPI} - 1)/2$ ratio curves can be created from the set of N_{PPI} hourly radial accumulation curves. Vignal and Krajewski (2001) rightfully argue that there is some redundancy between all those ratio curves and that it is not necessary to compute all of them. They only compute $N_{PPI} - 1$ ratio curves, all of them being relative to the lowest elevation angle. Here, all ratio curves are computed in order to maximize the amount of data used to retrieve the VPR. Another reason to do so arises from the difficulty in adequately selecting the reference rainfall accumulation radial curve with respect to which all ratios are going to be computed. Indeed, low-elevation data may be strongly affected by ground clutter or strong beam blockage and the corresponding radial accumulation curve may present a lot of missing data. On the other hand, selecting a high-elevation angle as the reference may not be optimal either as the beam is likely to overshoot the echo tops beyond some range, which here again induces missing slices in the corresponding rainfall accumulation ratio curve. Overall, computing all $N_{PPI}(N_{PPI} - 1)/2$ avoids dealing with the "single reference" problem while being neither particularly computationally expensive nor complex.

A ratio curve [$\rho_{OBS}(\theta_{UPP}, \theta_{LOW}, r)$] between two any elevation angles (θ_{UPP}, θ_{LOW}) is only computed if the corresponding upper and lower radial accumulation curves [$\Re(\theta_{UPP}, r)$ and $\Re(\theta_{LOW}, r)$] have been obtained from a sufficient and comparable number of pixels. This is necessary in order to obtain smooth and physical ratio curves.

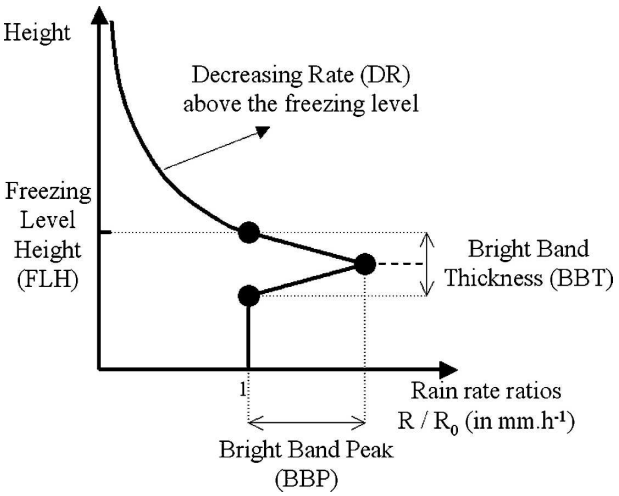

FIG. 5. Conceptualization of the VPR.

2) STEP 2: GENERATION OF THE SET OF VPR CANDIDATES

The VPR identification method relies on a simple conceptualization of the VPR with a limited number of parameters. Four parameters have been identified:

- freezing-level height (FLH), which represents the top of the bright band and is expressed in meters; notice that all heights hereafter are relative to the radar altitude;
- brightband peak (BBP), which is the ratio between the maximum enhanced rain rate and the surface rain rate; there is no unit applied since it is a ratio of rain rates (expressed in millimeters per hour);
- brightband thickness (BBT), which is expressed in meters; and
- decreasing rate above the freezing-level height (DR), which is usually expressed in decibels per kilometer.

Figure 5 summarizes the shape of the conceptual VPR. Notice that by convention in this paper the VPR is expressed in terms of rain-rate ratio. All four parameters are assumed to be independent of each other. Low-level (i.e., below the bright band) growth or evaporation of precipitation is not considered in the VPR conceptualization. Despite the fact that such low-level features might be quite important in some situations or geographical contexts (Kitchen et al. 1994; Kitchen 1997; Pellarin et al. 2002), they are usually dif-

ficult to assess in a robust manner with a scanning radar due to the presence of ground clutter and beam blocking in the lowest-elevation scans. As pointed out by Germann and Joss (2002), this lack of robustness is not acceptable from an operational point of view considering the impact that the low-level slope has on the rainfall estimation over the entire image. In addition, the low-level shape of the VPR is often highly variable in space. For instance, low-level growth (evaporation) usually takes place over the windward (leeward) slopes. The proposed VPR identification scheme assumes the horizontal uniformity of the VPR and cannot therefore account for such a spatial variability.

The bright band is assumed to extend by BBT below the freezing level (FLH). The brightband peak (BBP) is reached at FLH − BBT/2, that is, right in the middle of the bright band. The bright band is assumed to be symmetrical around FLH − BBT/2. The VPR (expressed as a ratio between the rain rate at a given altitude and the rain rate at ground level) is equal to 1 at the top and at the bottom of the bright band.

Above the bright band, the VPR is assumed to be exponentially decreasing, the decreasing rate (DR expressed as usual in decibels per kilometer) being constant with height. Unlike Kitchen (1997), we do not partition the upper part of the profile into two sections, one between FLH and, say, FLH + 2000 m and another above. Such a partition is supported by observations (Fabry and Zawadzki 1995) and physical considerations (aggregation of solid particles takes place above −6°C, i.e., in a ~1000 m thick layer above FLH) but it makes the VPR retrieval more complex. With DR (expressed in units of decibels per kilometer), the VPR above FLH (expressed as a rain-rate ratio) is given by

$$\begin{aligned} \mathrm{VPR}(z) &= \mathrm{VPR}(\mathrm{FLH})10^{[\mathrm{DR}(z-\mathrm{FLH})/(10b)]} \\ &= 10^{[\mathrm{DR}(z-\mathrm{FLH})/(10b)]}, \end{aligned} \tag{15}$$

where b is the exponent of the Z–R relationship (b = 1.6). Table 2 gives some typical values of the DR, BBP, and BBT parameters of the conceptual VPR. To further investigate the relevance of the proposed VPR conceptualization, and to assess the range of variation of the parameters, a climatological study was carried out on eight radars within the French radar network with different antenna characteristics, wavelengths, scanning strategies, and physical environments (Arcis/Aube, Sembadel, Plabennec, Bordeaux, Toulouse, Grèzes, Opoul, and Collobrières). The methodology and the results are presented in Part II. Overall, the VPR model is quite relevant in the sense that it is able to account for the variability of the ratio curves. Part II also investigates the statistical distribution of each of the shape parameters. Based on the results of that climatology, the whole VPR family is obtained by letting the parameters vary as follows:

- FLH: three values equal to $\mathrm{FLH}_0 - 200$, FLH_0, and $\mathrm{FLH}_0 + 200$, where FLH_0 is the model-predicted freezing-level height (relative to the radar altitude). The ±200 m range was tuned so as to account for typical model forecast errors. The advantages of using a first guess for FLH are 1) the avoidance of gross errors in the real-time determination of the brightband height and 2) the significant reduction of the computing time.
- BBP: five values equal to 1, 2, 3, 4, and 5 (expressed as a ratio of rainfall rates).
- BBT: four values equal to 200, 400, 600, and 800 m.
- DR: four values equal to −1.5, −3, −4.5, and −6 dB km^{-1}.

This makes a maximum number of 240 VPR candidates. A typical convective profile has a BBP equal to 1 and a DR equal to −1.5 dB km^{-1}.

3) STEP 3: SELECTION OF THE OPTIMAL VPR AND COMPUTATION OF THE CORRECTION FACTORS

The selection of the optimal VPR is done by generating $N_{\mathrm{PPI}}(N_{\mathrm{PPI}} - 1)/2$ simulated ratio curves $[\rho_{\mathrm{SIM}}(\theta_{\mathrm{UPP}}, \theta_{\mathrm{LOW}}, r)]$ and comparing them to the observed ratio curves. The computation of the simulated ratio between two elevation angles (θ_{LOW} and θ_{UPP}) at a given distance r and for a given VPR candidate takes into account the exact antenna diagram:

$$\rho_{\mathrm{SIM}}(\theta_{\mathrm{UPP}}, \theta_{\mathrm{LOW}}, r) = \mathrm{VPR\_app}(\theta_{\mathrm{UPP}}, r)/\mathrm{VPR\_app}(\theta_{\mathrm{LOW}}, r), \tag{16}$$

where $\mathrm{VPR\_app}(\theta_{\mathrm{UPP}}, r)$ and $\mathrm{VPR\_app}(\theta_{\mathrm{LOW}}, r)$ are the so-called apparent rain-rate VPR (Andrieu et al. 1995). They read

$$\mathrm{VPR\_app}(\theta_i, r) = \left\{ \left[\int_{\theta=\theta_i-2\Delta\theta}^{\theta=\theta_i+2\Delta\theta} \mathrm{VPR}(\theta)^b P^2(\theta)\, d\theta \right] \Big/ \left[\int_{\theta=\theta_i-2\Delta\theta}^{\theta=\theta_i+2\Delta\theta} P^2(\theta)\, d\theta \right] \right\}^{1/b}, \tag{17}$$

TABLE 2. Typical values of the four parameters used in the conceptual VPR model.

Reference	Data used	Retrieval method	Decreasing rate above the bright band (DR, dB km^{-1})	Brightband thickness (BBT, m)	Brightband peak (BBP expressed as a rain-rate ratio)
Koistinen (1991)	15 daily mean profiles	Use of volume data up to 45 km; beam-filtering effects are not taken into account	Range of variation: $-7.5 \rightarrow -12$ Mean value: -9.6	≈500	Up to 2 (+5 dB in terms of reflectivity enhancement)
Fabry and Zawadzki (1995)	600 h of vertically pointing radar data	Direct observation	Range of variation: $-6 \rightarrow -7$	$150 \rightarrow 800$ Mean value: 300	Around 4.2 (+10 dB in terms of reflectivity enhancement)
Joss and Lee (1995)	8 yr of VPR climatology obtained from Swiss radar data	Use of volume data up to 70 km; beam-filtering effects are not taken into account	With $b = 1.5$ in the $Z = aR^b$ relationship Summer mean: -2.4 (-1.6 dB R km^{-1}) Winter mean: -3.5 (-2.3 dB R km^{-1})	Estimated by Joss and Lee (1995) to be typically less than ≈ 300	Not documented
Novak and Kracmar (2001)	4 yr of VPR climatology obtained from the Czech Skalky radar	Use of volume data up to 70 km; beam-filtering effects are not taken into account	Range of variation: $-2 \rightarrow -7$ Mean value: -4	≈1000	Up to 3.6 (+9 dB in terms of reflectivity enhancement)
Kitchen (1997)	3 months of RHI scans from the Chibolton radar	Retrieval of some parameters of a conceptual VPR through the computation of ratio curves; beam-filtering effects are taken into account	Range of variation: $0 \rightarrow -20$ Mean value: -6	Set by the method to the fixed value of 500	BBP is parametrized as a function of the rain reflectivity below the brightband 1.7 for $Z_{\mathrm{RAIN}} = 10$ dBZ 2.5 for $Z_{\mathrm{RAIN}} = 20$ dBZ 4.2 for $Z_{\mathrm{RAIN}} = 30$ dBZ
Vignal and Krajewski (2001)	2 yr of VPR climatology obtained from the Tulsa, OK, WSR-88D radar	Inverse method based on the computation of ratio curves; beam-filtering effects said to be taken into account	Range of variation: $-1 \rightarrow -7$ Mean value: -3 Stratiform mean: -4 Convective mean: -3	≈1000	Up to 3.6 (+9 dB in terms of reflectivity enhancement) Mean value: 1.4 (+2.5 dB)

where $\theta_i = \theta_{\mathrm{LOW}}, \theta_{\mathrm{UPP}}$, $\Delta\theta$ the half 3-dB beamwidth, and $P(\theta)$ is the one-way antenna diagram. The b and $1/b$ exponents arise from the fact that the VPRs are by convention expressed in terms of rain rates and not reflectivity (in linear units) in this paper. The integration is actually achieved in a discrete way along the vertical, the vertical integration step being 100 m, that is, the resolution of the VPR. Several examples of observed and simulated ratio curves are presented in Part II. The quadratic error between the observed and simulated ratios is then used as the score to select the optimal VPR. The following cost function is proposed:

$$\mathrm{QE}(i_{\mathrm{VPR}}) = \sum_{\theta\mathrm{INF}=1}^{\mathrm{NPPI}} \sum_{\theta\mathrm{SUP}>\theta\mathrm{INF}}^{\mathrm{NPPI}} \sum_{r=1}^{r\,\max} \delta(\theta_{\mathrm{UPP}}, \theta_{\mathrm{LOW}}, r)[\rho_{\mathrm{OBS}}(\theta_{\mathrm{UPP}}, \theta_{\mathrm{LOW}}, r) - \rho_{\mathrm{SIM}}(\theta_{\mathrm{UPP}}, \theta_{\mathrm{LOW}}, r)]^2, \quad (18)$$

where $\delta(\theta_{LOW}, \theta_{UPP}, r)$ is equal to 1 if the observed ratio is available and 0 otherwise. The VPR is not retrieved if not enough ratios $\rho_{OBS}(\theta_{UPP}, \theta_{LOW}, r)$ are available. In that case, a so-called climatological VPR is used [-1.5 dB km^{-1}, as in Joss and Lee (1995)].

The correction factors, denoted by $\beta_k(i, j)$ in Fig. 2, only depend upon the elevation angle and the radial distance. For a given elevation angle θ and a radial distance r, the correction factor is simply the inverse of VPR_app(θ, r), as calculated in Eq. (17).

The weights update formula only depends upon the height of the pixel above the underlying terrain and not upon the VPR. The proposed relationship is exponential as in Joss and Lee (1995):

$$\omega_k(i,j) \leftarrow \omega_k(i,j)\exp\{-[h - h_{terrain}(i,j)]/h_0\} \quad \text{if} \quad h - h_{terrain}(i,j) < 10\ \text{km} \quad \text{and} \tag{19}$$

$$\omega_k(i,j) \leftarrow 0 \quad \text{if} \quad h - h_{terrain}(i,j) > 10\ \text{km}. \tag{20}$$

Quite expectedly, the weight is rapidly decreasing with height. In that empirical formula, h_0 is a parameter that controls the decreasing rate of the weight with height. A small h_0 value will lead to a rapid decrease of the weight with height and the final weighted linear combination will actually be reduced to picking the lowest-elevation angle. On the other hand, a large h_0 value will lead to more vertical integration. The optimal h_0 value should actually be set according to what is known about the statistical quality of the radar surface rainfall rate estimation as a function of height. This clearly depends on the type of rain (stratiform–convective). However, on average and even though a VPR correction is applied, it is clear that a 1-km rise of the height from which the surface rainfall estimation is obtained already yields a significant deterioration of the quality.

It should also be noted that the setting of h_0 is related to the weight update formula that has been used in the partial beam-blocking correction module [Eqs. (11) and (12)]. Indeed, in complex terrain, one is often faced with the problem of choosing between a low, partially blocked, elevation angle measurement that has been corrected for partial beam blocking and a higher, unblocked elevation angle measurement that has been corrected for VPR effects. Another way to state the problem is, In the weighted linear combination, what weights should be assigned to each of the two measurements to get the best estimation? If the partial beam-blocking correction scheme were perfect, then the lowest-elevation angle measurement should always be favored and h_0 should be set to a very small value. On the other hand, if the VPR could be known with perfect accuracy, then unshielded data, whatever their heights, should always be preferred, which would be introduced in the processing chain by strongly diminishing the weights of the shielded data.

However, neither correction procedure is perfect and a trade-off has to be found. Figure 6 shows the relative weights of the high- and low-elevation angle measurements as a function of the percentage of blocking of the lowest elevation and the height difference between the two elevations. The higher elevation is always assumed to be unblocked (even when the height difference tends to zero). The weights update formula that have been used are the ones given by Eqs. (11)–(12) and (19)–(20). Here, h_0 has been set to 1 km. The thick line represents the equality line (i.e., the two measurements have exactly the same weight) and the two thin lines above and below correspond, respectively, to ω_high = 0.5ω_low and ω_high = 2ω_low. The letters U (L) indicate the region where the upper- (lower-) elevation angle is dominant in the weighted linear combination. For instance, if the lowest-elevation angle is shielded by 50%, then it will have the same weight as an unblocked measurement that is located about 400 m higher. If the upper-elevation measurement is 1000 m higher- then its weight will be half of that of the lower-elevation angle. Beyond 70% occulation, the weight of the lower-elevation angle is set to zero and the upper-elevation measurement becomes dominant. Overall, that empirical setting appears to be reasonable.

e. Synchronization

Once corrected for ground clutter, partial beam blockage, and VPR effects, the set of PPIs obtained during the 5-min period of the sampling cycle has to be synchronized before being combined. Advection can be quite important in a number of situations such as cases involving convective lines or frontal systems and values as large as 20 m s^{-1} have already been observed. In such cases, a difference of 5 min in the PPI collection results in a spatial gap of more than 5 km, so that the vertical column above each surface pixel appears to be completey distorted.

Two-dimensional advection fields, the components of which are denoted by $U_{adv}(i, j)$ and $V_{adv}(i, j)$, are computed in real time every 5 min using a standard cross-correlation approach (as in Tuttle and Foote

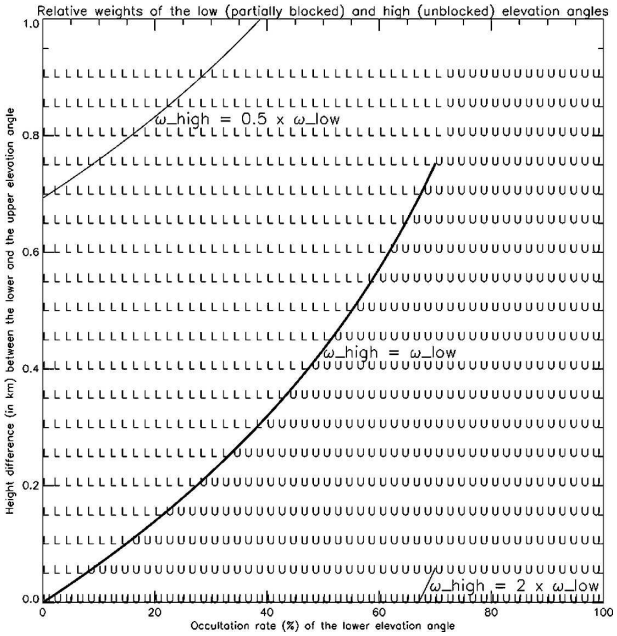

FIG. 6. Relative weights of the low, partially blocked and high, unblocked elevation angles as a function of the percentage of blocking of the low elevation and height difference between the two measurements. The weights update formula for the partial beam blocking and VPR correction modules are, respectively, given in Eqs. (11) and (12) and (19) and (20). The thick line corresponds to equality between the two weights and the two thin lines above and below correspond, respectively, to $\omega\_high = 0.5\omega\_low$ and $\omega\_high = 2\omega\_low$. The letter L (U) indicates the region where the lower- (higher-) elevation angle measurement is dominant in the weighted linear combination.

1990). A pixel located at (i, j) and measured at time t is synchronized with respect to a common reference time t_0 (say, the beginning of the 5-min period) is processed as follows:

$$i_0 = i - (t - t_0)U_{\text{adv}}(i, j), \tag{21}$$

$$j_0 = j - (t - t_0)V_{\text{adv}}(i, j), \quad \text{and} \tag{22}$$

$$R_k(i_0, j_0) \leftarrow R_k(i, j) \quad \text{and} \quad \omega_k(i_0, j_0) \leftarrow \omega_k(i, j), \tag{23}$$

where i_0 and j_0 are the new coordinates of the pixel after synchronization.

f. Weighted linear combination

Once synchronized, all PPIs gathered within the 5-min time period are combined on a pixel-by-pixel basis to yield the best surface rainfall estimation. Following Joss and Lee (1995), data are combined in a weighted linear fashion. The weights that are used in this final estimation are the quality indexes that have been updated after each module of the processing chain $[\omega_k(i, j)]$:

$$R_{\text{best}}(i, j) = \sum_k \omega_k(i, j) R_k(i, j) \Big/ \sum_k \omega_k(i, j). \tag{24}$$

The final values of the quality indexes may also be used to infer a rough estimate of the quality of the surface rainfall rate. Such information may be useful for forecasters, radar–rain gauge comparisons, model verification, mosaicking, etc. The set of quality index PPIs has to be combined somehow to provide a 2D field. We propose using the maximum value that entered into the weighted linear combination as a proxy:

$$\omega_{\text{estimated}}(i, j) = \text{MAX}_k[\omega_k(i, j)]. \tag{25}$$

This choice is clearly arbitrary and other integration formulas may have been proposed.

g. 5-min rainfall accumulation

The final step of the processing chain consists of generating a 5-min rainfall accumulation from the instantaneous surface rainfall rate estimation at t_0. To achieve this, the surface rainfall rate estimation at t_0 is advected using the advection field for a second time by 1-min increments to provide extrapolated rainfall rates fields at $t_0 + 1$, $t_0 + 2$, $t_0 + 3$, and $t_0 + 4$. The 5-min rainfall accumulation is then obtained as a simple sum over the set of five rainfall rate fields $[R_{\text{best}}(i, j), R_{\text{best}}(i, j)^{t_0 \to t_0+1}, R_{\text{best}}(i, j)^{t_0 \to t_0+2}, R_{\text{best}}(i, j)^{t_0 \to t_0+3}, R_{\text{best}}(i, j)^{t_0 \to t_0+4}]$:

$$C(i, j) = (1/60)[R_{\text{best}}(i, j) + R_{\text{best}}(i, j)^{t_0 \to t_0+1} + R_{\text{best}}(i, j)^{t_0 \to t_0+2} + R_{\text{best}}(i, j)^{t_0 \to t_0+3} + R_{\text{best}}(i, j)^{t_0 \to t_0+4}], \tag{26}$$

with $C(i, j)$ being expressed in millimeters and the rainfall rates in millimeters per hour (hence the 1/60 factor). This oversampling allows for the smoothing of the rainfall accumulation map and the suppression of stroboscopic effects that are often visible in the case of rapidly moving systems. The quality index assigned to the 5-min rainfall accumulation field is the one determined previously in Eq. (25).

If the weights of all available measurements at the vertical of a given pixel are equal to zero, which can happen if at that point all elevation angles of the VCP are affected by ground clutter, then that pixel is replaced by the extrapolation of a valid pixel taken from a previous image. The weight of the replaced pixel is changed to the weight of the extrapolated pixel. This procedure allows us to fill out areas of missing data and

gives much better results than a simple spatial interpolation in the case of moving convective cells.

4. Conclusions

The new French operational radar rainfall product has been presented in this paper. The processing chain is made of a series of modules that correct for ground clutter, partial beam blocking, VPR effects, and advection. Emphasis is placed on simplicity and robustness as the algorithm is meant to be deployed within the French operational radar network.

Ground-clutter pixels are identified in real time using the pulse-to-pulse fluctuation of the radar reflectivity.

Partial beam blocking is corrected for by the use of numerical simulations of the interaction between the radar wave and its environment. Nonorogenic masks are not accounted for in the current version of the algorithm. Another weakness of the current version is the fact that the blocking correction is not coupled with the VPR correction. It was shown that this could lead to significant underestimations of the correction factors even at moderate ranges from the radar.

The VPR identification module relies on hourly rainfall accumulation ratio curves and on VPR candidates. The beam-filtering effect is taken into account in the retrieval. The VPR identification module is specifically validated in Part II. Before being combined, PPIs gathered within the 5-min window are synchronized in real time by means of a cross-correlation field. Each pixel of each PPI has a quality index that is updated after each module according to the amount and/or accuracy of the correction that is performed. In the current version of the algorithm, the quality index essentially depends upon the presence of ground clutter, the degree of blocking, and the altitude. The weighted update formulas are empirical but quite consistent with common sense. The final QPE product is obtained on a pixel-by-pixel basis as a weighted sum over all available PPIs, using the final quality indexes as weigting factors. Results of the comparison of the final radar QPE are discussed in Part II, which also assesses the relevance of the proposed quality indexes to account for radar–rain gauges differences.

Acknowledgments. This work was done within the framework of the French Project Programme ARAMIS Nouvelles Technologies en Hydrométéorologie Extension et Renouvellement (PANTHERE) supported by Météo-France, the French Ministère de l'Ecologie et du Développement Durable, and the European Regional Development Fund (ERDF) of the European Union. This work would not have been possible without the contributions of Kim Do Khac and Laurent Périer (Météo-France), who developed the new CASTOR2 radar processor. Finally, I would like to acknowledge Vincent Debaecker for his significant input on the implementation and scientific validation of SURFILLUM, Françoise Eideliman for developing the radar QPE code, and Jacques Parent-du-Châtelet for his support.

REFERENCES

Anagnostou, E. N., and W. Krajewski, 1999: Real-time radar rainfall estimation. Part I: Algorithm formulation. *J. Atmos. Oceanic Technol.,* **16,** 189–197.

Andrieu, H., and J. D. Creutin, 1995: Identification of vertical profiles of radar reflectivity for hydrological applications using an inverse method. Part I: Formulation. *J. Appl. Meteor.,* **34,** 225–239.

——, G. Delrieu, and J. D. Creutin, 1995: Identification of vertical profiles of radar reflectivity for hydrological applications using an inverse method. Part II: Sensitivity analysis and case study. *J. Appl. Meteor.,* **34,** 240–259.

Delrieu, G., J. D. Creutin, and H. Andrieu, 1995: Simulation of radar mountain returns using a digitized terrain model. *J. Atmos. Oceanic Technol.,* **12,** 1038–1049.

Dinku, T., E. N. Anagnostou, and M. Borga, 2002: Improving radar-based estimation of rainfall over complex terrain. *J. Appl. Meteor.,* **41,** 1163–1178.

Fabry, F., and I. Zawadzki, 1995: Long-term radar observations of the melting layer of precipitation and their interpretation. *J. Atmos. Sci.,* **52,** 832–851.

Fulton, R. A., J. P. Breidenbach, D.-J. Seo, D. A. Miller, and T. O'Bannon, 1998: The WSR-88D rainfall algorithm. *Wea. Forecasting,* **13,** 377–395.

Germann, U., and J. Joss, 2002: Mesobeta profiles to extrapolate radar precipitation measurements above the Alps to the ground level. *J. Appl. Meteor.,* **41,** 542–557.

Joss, J., and R. Lee, 1995: The application of radar–gauge comparisons to operational precipitation profile corrections. *J. Appl. Meteor.,* **34,** 2612–2630.

Kitchen, M., 1997: Towards improved radar estimates of surface precipitation rate at long range. *Quart. J. Roy. Meteor. Soc.,* **123,** 145–163.

——, R. Brown, and A. G. Davies, 1994: Real-time correction of weather radar data for the effects of bright band, range and orographic growth in widespread precipitation. *Quart. J. Roy. Meteor. Soc.,* **120,** 1231–1254.

Koistinen, J., 1991: Operational correction of radar rainfall errors due to the vertical reflectivity profile. Preprints, *25th Int. Conf. on Radar Meteorology,* Vol. I, Paris, France, Amer. Meteor. Soc., 91–94.

Novak, P., and J. Kracmar, 2001: Vertical reflectivity profiles in the Czech Weather Radar Network. Preprints, *30th Int. Conf. on Radar Meteorology,* Munich, Germany, Amer. Meteor. Soc., CD-ROM, P15.3.

Parent-du-Châtelet, J., and M. Guiméra, 2003: The PANTHERE project of Météo-France: Extension and upgrade of the French radar network. Preprints, *31st Conf. on Radar Meteorology,* Seattle, WA, Amer. Meteor. Soc., 802–804.

——, and Coauthors, 2001: CASTOR2, a new computer for the French radar network. Preprints, *30th Int. Conf. on Radar*

Meteorology, Munich, Germany, Amer. Meteor. Soc., CD-ROM, P2.14.

Pellarin, T., G. Delrieu, G. M. Saulnier, H. Andrieu, B. Vignal, and J. D. Creutin, 2002: Hydrologic visibility of weather radar systems operating in a mountainous region: Case study for the Ardèche catchment (France). *J. Hydrometeor.,* **3,** 539–555.

Sugier, J., J. Parent-du-Châtelet, P. Roquain, and A. Smith, 2002: Detection and removal of clutter and anaprop in radar data using a statistical scheme based on echo fluctuation. *Proc. Second European Radar Conf.,* Delft, Netherlands, Copernicus GmbH, 17–24.

Tabary, P., 2003: Efforts to improve the monitoring of the French radar network. Preprints, *31st Int. Conf. on Radar Meteorology,* Seattle, WA, Amer. Meteor. Soc., CD-ROM, P3C.9.

——, F. Guiber, L. Périer, and J. Parent-du-Châtelet, 2006: An operational triple-PRT Doppler scheme for the French radar network. *J. Atmos. Oceanic Technol.,* **23,** 1645–1656.

——, J. Desplats, K. Do Khac, F. Eideliman, C. Gueguen, and J.-C. Heinrich, 2007: The new French operational radar rainfall product. Part II: Validation. *Wea. Forecasting,* **22,** 409–427.

Testud, J., E. Le Bouar, E. Obligis, and M. Ali-Mehenni, 2000: The rain profiling algorithm applied to polarimetric weather radar. *J. Atmos. Oceanic Technol.,* **17,** 332–356.

Tuttle, J. D., and G. B. Foote, 1990: Determination of boundary layer airflow from a single Doppler radar. *J. Atmos. Oceanic Technol.,* **7,** 218–232.

Vignal, B., and F. W. Krajewski, 2001: Large-sample evaluation of two methods to correct range-dependent error for WSR-88D rainfall estimates. *J. Hydrometeor.,* **2,** 490–504.

——, G.-M. Galli, J. Joss, and U. Germann, 2000: Three methods to determine profiles of reflectivity from volumetric radar data to correct precipitation estimates. *J. Appl. Meteor.,* **39,** 1715–1726.

Zawadzki, I., 1984: Factors affecting the precision of radar measurements of rain. Preprints, *22d Int. Conf. on Radar Meteorology,* Zurich, Switzerland, Amer. Meteor. Soc., 251–256.